Chaos control of a shape memory alloy structure using thermal constrained actuation

Dimitri D.A. Costa [a], Marcelo A. Savi [a,*], Aline S. de Paula [b], Davide Bernardini [c]

[a] *Center for Nonlinear Mechanics, COPPE–Department of Mechanical Engineering, Universidade Federal do Rio de Janeiro, 21.941.972–Rio de Janeiro–RJ, P.O. Box 68.503, Brazil*
[b] *Department of Mechanical Engineering, Universidade de Brasília, 70.910.000-Brasília–DF, Brazil*
[c] *Department of Structural and Geotechnical Engineering Università di Roma-La Sapienza, Via Antonio Gramsci 53, 00197, Rome, Italy*

ARTICLE INFO

ABSTRACT

Shape memory alloys (SMAs) have been widely used in smart structures due to their adaptive properties. Their thermomechanical coupling can provide vibration attenuation or actuation providing a desired dynamical response. Chaos control methods can provide the stabilisation of unstable periodic orbits allowing one to choose a convenient response. Besides, it can promote bifurcation control that can avoid undesirable responses. This work investigates the chaos control of smart structures employing time-delayed feedback control to perform orbit stabilisation. A two-bar truss is of concern using thermal actuation of SMA elements. Thermal constraints defined by energy equation are investigated, showing the real possibilities of this kind of control. Numerical results show situations related to controller constraints, defining its range of applicability. Control strategy potentialities are discussed showing unstable periodic orbit stabilisation, exchangeable target control and bifurcation control.

1. Introduction

Smart structures are being employed in different situations due to their adaptive behaviour. In this regard, shape memory alloys (SMAs) constitute an interesting alternative when large forces and displacements are required. SMAs present thermomechanical couplings due to solid phase transformations. In brief, these transformations lead to two main behaviours: shape memory effect, which is the ability to recover a mechanical induced residual strain using a thermal load; and pseudoelasticity, a phenomenon where phase transformation induces large recoverable strains, presenting a hysteresis loop.

The use of SMA elements in mechanical systems can attenuate vibrations [1], change structure configurations [2,3], mimic natural movements [4], promote actuation [5,6] among other applications.

Dynamical applications of SMA tend to be related to complex responses. SMA dynamical response is associated with a temperature dependent hysteretic behaviour that can change equilibrium point structure, leading to complex behaviours that include chaos. In this regard, the use of SMA elements on smart material systems needs to be preceded by a deep nonlinear dynamics analysis and control strategies can be useful to avoid undesirable responses. Savi [7] presents a general overview of SMA dynamical systems.

The two bar-truss is an archetypal model to represent different kinds of frame structures and flat arches, being employed to analyse stability

of such structures. Concerning its nonlinear dynamics, the two-bar truss has complex behaviours related to geometrical nonlinearities and it should be highlighted snap-through and chaos [8]. The SMA two-bar truss combines geometrical and constitutive nonlinearities, being of special interest for aerospace applications. Savi et al. [9] and Savi and Nogueira [10] previously addressed the dynamical analysis of SMA two-bar truss considering different constitutive models.

Chaos control has the main goal to stabilise unstable periodic orbits (UPOs) embedded on chaotic attractors using small perturbations. This approach allows one to exploit chaotic behaviour, by stabilising desirable orbits and conferring flexibility to the system since it is possible to change from one orbit to another with low power consumption [11,12]. Another possibility related to chaos control technique is the bifurcation control that can avoid undesirable responses [13–15].

Chaos control methods can be classified in discrete and continuous techniques [11,16]. The extended time-delayed feedback control (ETDF) [17] is one of these continuous approach that has been implemented on different situations and explored by various authors [18–20]. Mechanical systems is one of the tested possibilities [21], as well as smart structures [14,22,23].

This paper deals with chaos and bifurcation control of an SMA two-bar truss. The literature presents some investigations of the SMA two-bar truss control [14,24]. Nevertheless, these contributions do not take

---

advantage of the SMA adaptive behaviour on the controller, using some different actuation approach. This work employs thermal actuation as the control parameter. The extended time delayed feedback control is employed and the control strategy is used either to suppress the chaotic behaviour or to avoid bifurcations. Heat transfer constraints are incorporated on the controller, establishing two different scenarios: an ideal controller, where thermal actuation has no constraints; and a constrained controller, where heat transfer limits SMA actuation. A comparison between them is of concern establishing situations where the desired control is achieved. Costa and Savi [23] also discussed thermal actuation for chaos control considering a different dynamical system. The present work focuses on a structural system, discussing aspects related to chaos control as unstable periodic orbit stabilisation, target exchange and bifurcation control.

2. Control method

Chaos control is a two stage approach composed by a learning stage, where UPOs are identified and controller parameters are defined; and a stabilisation stage, where UPO stabilisation is performed. A general overview of chaos control methods and a comparative analysis of their capability to stabilise a desired UPO can be found in [25], and [12].

The extended time-delayed feedback control method (ETDF) [17] is an interesting continuous approach that has been successfully employed in various experimental applications in electrical and mechanical systems [14,21,23,26–29]. In brief, the system dynamics is represented by the following equations,

$$\dot{x} = f(x, t) + g(y(t), y(t - \tau), y(t - 2\tau), \ldots)$$
$$y(t) = C(x) \tag{1}$$

where $x \in \mathbb{R}^N$ is the system state, t is the time, $f(x, t) \in \mathbb{R}^N$ defines the system dynamics and $(\dot{\ })$ represents time derivatives; $y \in \mathbb{R}^M$ is the system observation provided by the operator $C(x) \in \mathbb{R}^M$; $g \in \mathbb{R}^N$ is the control signal defined as follows

$$g(y, t) = K \left[[1 - R] \sum_{n=1}^{\infty} R^{n-1} y(t - n\tau) - y(t) \right] \tag{2}$$

where $K \in \mathbb{R}^{N \times M}$ is a proportional gain and $R \in \mathbb{R}$ is a controller parameter; τ is the period of the target UPO to be controlled. Note that, when the orbit tends to a target period-τ UPO, Eq. (2) tends to zero since $y(t - n\tau) \rightarrow y(t)$.

Control parameters K and R are defined from the analysis of the UPO stability under control action. In this regard, either Lyapunov exponents [14,21,29] or Floquet exponents [28,30] can be employed.

In this work, Floquet exponents are employed to analyse the stability of the UPOs and set the parameters K and R following the procedures presented in references [23] and [28]. By considering a displacement $\delta x(t) = x(t) - x_0(t)$ of a target UPO, $x_0(t)$, Floquet theory gives the solution for the linear approximation given by:

$$\delta x(t) = \text{Re} \left(\sum_{i=1}^{N} \left[\delta x(0) \cdot p_i(0) \right] e^{\mu_i t} p_i(t) \right) \tag{3}$$

where $p_i(t) = p_i(t + \tau)$ is a periodic orbit that has the same period of the UPO and $\mu_i \in \mathbb{C}$ are the UPO Floquet exponents; dot represents inner product.

Eq. (3) shows that the Floquet exponents govern the deviation from the UPO. Therefore, if all exponents have a negative real part, δx decreases over time and tends to vanish for $t \rightarrow \infty$, indicating the UPO stability. On the other hand, if any Floquet exponent has a positive real part, δx increases over time and the solution diverges from the orbit. Thus, the maximum real value of the Floquet exponent, $\text{Re}(\mu_{max}) = \max \left(\text{Re}(\mu_i) \right)$, defines the UPO stability. If $\text{Re}(\mu_{max}) < 0$, the orbit is stable, and if $\text{Re}(\mu_{max}) > 0$, the orbit is unstable.

Hence, controller parameters K and R can be adjusted by evaluating the Floquet exponents of a target UPO. Various methods can be used to calculate Floquet exponents. An optimisation method can estimate K

and R prior to the control application. It considers a time evolution linearisation around a reference path $x_0(t)$, which leads to a displacement $\delta x(t) = x(t) - x_0(t)$ of the path. Based on that, Eq. (1) can be linearised around an UPO using its Taylor expansion, leading to the evolution of the displacement δx given by:

$$\delta \dot{x}(t) = D f(t; x_0) \delta x(t) + K B \left[[1 - R] \sum_{n=1}^{\infty} R^{n-1} \delta x(t - n\tau) - \delta x(t) \right] \tag{4}$$

where $D f$ is the Jacobian matrix and B is the gradient of the function $C(x_0)$ with respect to its variables.

Since Eq. (4) has the form $\dot{x} = Ax$, with $A(t) = A(t + \tau)$ due to the fact that it is evaluated around a periodic orbit of period τ, Floquet theory establishes that:

$$\delta x(t) = e^{H(\mu)t} q(t) \tag{5}$$

where $q(t)$ is a period-τ function and $H(\mu) \in \mathbb{R}^{N \times N}$ is a matrix that has N Floquet exponents as eigenvalues. Under this assumption, delayed and present states are related as follows:

$$\delta x(t - n\tau) = e^{-Hn\tau} \delta x(t) \tag{6}$$

Eq. (6) allows one to calculate the infinite sum of Eq. (4), leading to:

$$\delta \dot{x}(t) = [D f(t; x_0) - K B [\mathbb{I} - e^{-H\tau}] [\mathbb{I} - R e^{-H\tau}]^{-1}] \delta x(t) \tag{7}$$

where $\mathbb{I}$ is the identity matrix. Note that Eq. (6) correlates delayed and present states reducing the dimension of Eq. (7) from infinity to the uncontrolled system dimension, N. Nevertheless, this reduction makes the displacement time evolution to be dependent on the Floquet exponents themselves.

The Floquet exponents are calculated by the evaluation of the eigenvalues of the fundamental matrix of the system after one period of time integration. In this regard, the definition of the fundamental matrix can be considered as:

$$\delta x(t) = \psi(t) \delta x(0) \tag{8}$$

where $\psi(t)$ is the fundamental matrix and $\psi(0) = \mathbb{I}$. The time evolution of the fundamental matrix can be obtained by using Eq. (8) on Eq. (7):

$$\dot{\psi} = \left[D f(t; x_0) - K B [\mathbb{I} - e^{-H\tau}] [\mathbb{I} - R e^{-H\tau}]^{-1} \right] \psi \tag{9}$$

By calculating $\psi(\tau)$, the Floquet exponents that depends of controller parameters K and R, can be obtained by solving the transcendental equation:

$$\psi(\tau; \mu) - e^{\mu_j \tau} \mathbb{I} = 0 \tag{10}$$

Note that Eq. (10) has an infinite number of solutions which reflects the infinite number of Floquet exponents. Besides, since Eq. (9) depends on the Floquet exponents themselves, an optimisation procedure is needed to solve it. In this regard, Floquet exponents are estimated using a differential evolution-based algorithm [31], presented on Fig. 1. This optimisation procedure on its kth iteration considers a population of trial values $\mu^{trial}[k]$ and apply it to the integration of Eq. (9) by using a fourth order Runge–Kutta method to obtain the fundamental matrixes $\psi(\tau; \mu^{trial}[k])$. Afterwards, the new Floquet exponents $\mu[k]$ are calculated by Eq. (10) and compared with the initial trials $\mu^{trial}[k]$ using an Euclidean metric, $\delta \mu$. This metric is then used to select the best individuals. Lower values of $\delta \mu$ indicate a high level of fitness and high probability to leave decedents. The stop criterion is defined if all individuals of the population satisfy a tolerance $\delta \mu < \delta_{tol}$. If this criterion is satisfied, the best individual μ^{best}, which has the lowest value of the metric $\delta \mu$, is chosen among the population. Otherwise, the algorithm due to Storn and Price [31] is employed to generate the new population $\mu^{trial}[k + 1]$.

Floquet exponents can also be verified from time series analysis. Although this approach cannot be used to set control parameters K and R, it is useful to evaluate the stability of an UPO. Its application requires
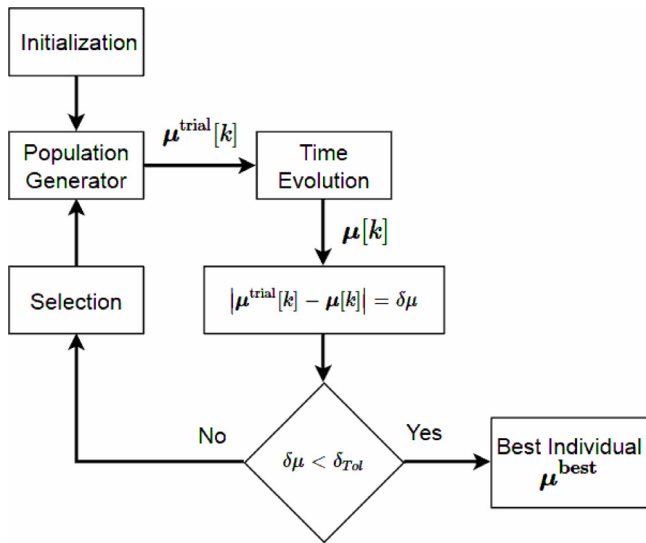
Fig. 1. Algorithm to calculate the Floquet exponents with ETDF control. $\mu^{trial}[k]$ indicates the kth population, $\mu[k]$ is the calculated Floquet exponent population after temporal evolution of the UPO's period, $\delta\mu$ is the fitness value, δ_{Tol} is the stopping criteria tolerance, and μ^{best} is the best individual on the selected population.
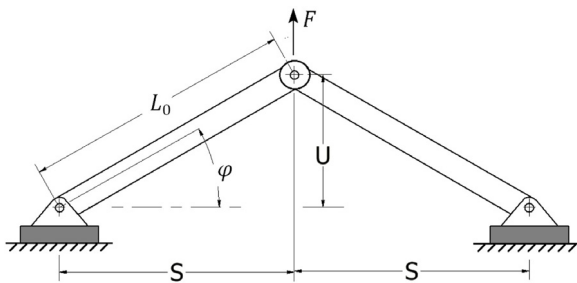
Fig. 2. Schematics of the two bar truss.
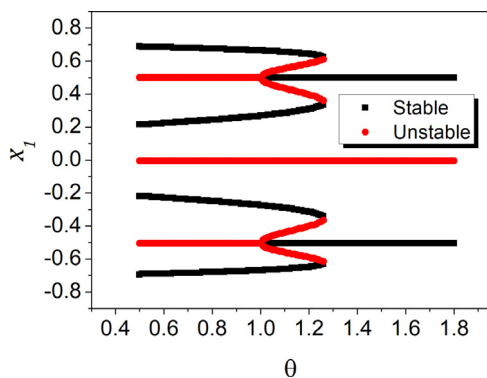
Fig. 3. Equilibrium point locus versus the dimensionless temperature θ.

that the system solution is close to the analysed orbit, which means that linear approximation of the displacement δx is valid (Eq. (3)). Floquet exponents can be calculated considering that p_i is a period-τ response ($p_i(\tau j) = p_i(0), j \in \mathbb{N}$), and therefore, by assuming a time series with the same periodicity ($t \to \tau j$), Eq. (3) can be reduced to:

$$\delta x[j] = \text{Re}\left(\sum_{i=1}^{N}[\delta x(0) \cdot p_i(0)] e^{\mu_i \tau j} p_i(0)\right) \tag{11}$$

where j is the time series index.

As $t \to \infty$, the term μ_{max} prevails among all other terms. Hence, the time series can be expressed as:

$$\delta x[j] \sim \text{Re}\left(A_{max} e^{i\tau j \mu_{max}}\right) = A_{max} e^{\text{Re}(\mu_{max})\tau j} \cos(\text{Im}(\mu_{max})\tau j) \tag{12}$$

Under these assumptions, Eq. (12) expresses the relation between the time series and μ_{max}, allows one to extract the Floquet exponents from the time series.

3. SMA two-bar truss mathematical model

The thermomechanical description of SMA is the objective of several research efforts being associated with a large number of constitutive theories. Lagoudas [32] and Paiva and Savi [33] presented a general overview of some of these efforts. The simplest model that can be properly employed for dynamical applications description is the one proposed by Falk [34] that assumes a polynomial stress–strain–temperature ($\sigma - \epsilon - T$) relation.

The definition of the polynomial constitutive theory is based on a temperature dependent sixth order polynomial Helmholtz free energy that can represent the stability of austenitic and martensitic phases at different temperatures. For low temperatures where martensite is stable at a stress-free state, there are two minima representing the two martensitic variants (tension-induced, M_+, and compression-induced, M_-). For intermediate temperature, the potential presents three minima indicating that both martensitic phases and austenite (A) can be stable. For high temperatures, the potential presents only one minimum indicating that austenite is the only stable on a stress-free state. Based on that, the stress–strain–temperature relation is given by:

$$\sigma = a_1[T - T_M]\epsilon - a_2\epsilon^3 + a_3\epsilon^5 \tag{13}$$

where a_1, a_2 and a_3 are material parameters, T_M is the temperature below with only martensitic phases are stable. By defining T_A as the temperature above with the polynomial potential has only one equilibrium point, it can be expressed as:

$$T_A = T_M + \frac{1}{4}\frac{a_2^2}{a_1 a_3} \tag{14}$$

This polynomial model presents a qualitative description of the SMA thermomechanical behaviour that is useful for some situation, especially dynamical purposes [35]. It should be pointed out that this model is not able to present a proper description of the hysteretic behaviour. Nevertheless, the polynomial model is useful for dynamical systems with SMA elements. A comparison between dynamical behaviour of SMA oscillators with SMA elements described with the polynomial model and more realistic models shows that both descriptions presents the same qualitative behaviour, meaning that the polynomial model together with a linear viscous dissipation is representative of the dynamical aspects of the SMA structural system [7,35]. Bernardini and Rega [36] evaluated the performance of different constitutive models in the nonlinear dynamics of pseudoelastic oscillators considering a comprehensive modelling framework.

The SMA structure is now of concern considering an SMA two-bar truss composed by two connected identical SMA bars with cross section A, free to rotate along their connection and their joint as can be seen on Fig. 2. The bars have an angle φ with the horizontal plane and their bases are separated by a distance $2S$. The system is considered to have a lumped mass m at the connection between the two bars, and a concentrated, external force $F(t)$ is applied to this connection. The equation of motion for the distance between the tip mass and the horizontal plane, U, is given by the following equation where a linear viscous dissipation, c, is incorporated to describe all system dissipations, including hysteretic dissipation:

$$m\ddot{U} = -2P\sin(\varphi) - c\dot{U} + F(t) \tag{15}$$

where $P = \sigma A$ is the reaction force of the SMA bar, which depends on their constitutive model.
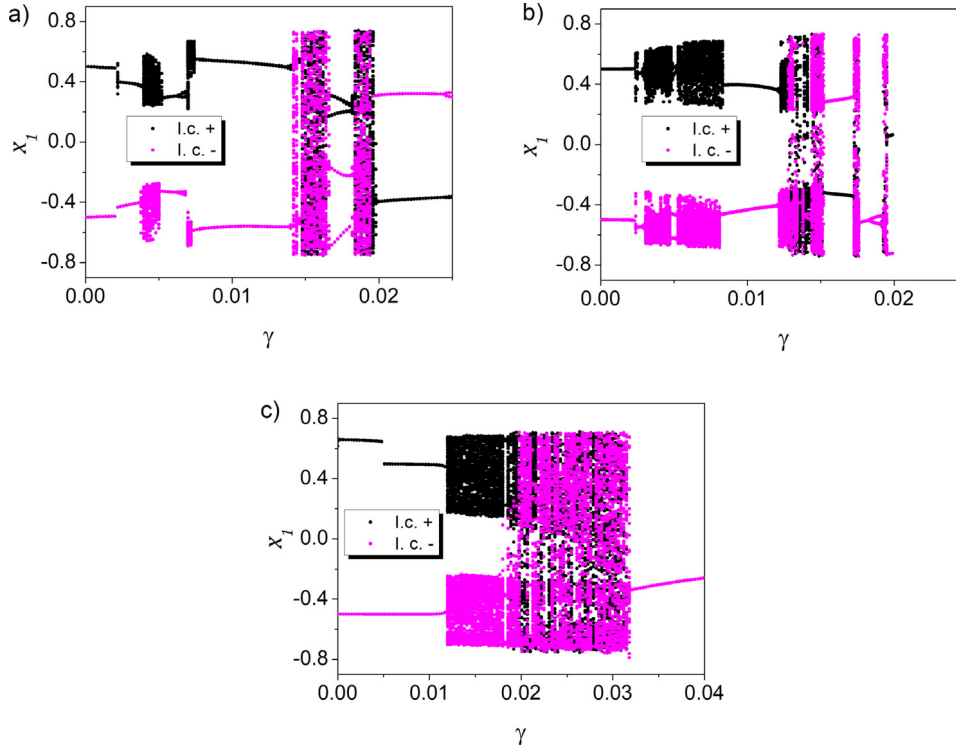
Fig. 4. Bifurcation diagrams varying γ. Positive initial conditions (I.c.+) in black and negative initial conditions (I.c.-) in magenta. (a) $\omega = 0.14$, $\theta = 1.3$ and $\zeta = 0.01$; (b) $\omega = 0.1$, $\theta = 1.3$ and $\zeta = 0.01$; (c) $\omega = 0.5$, $\theta = 1.1$ and $\zeta = 0.05$.
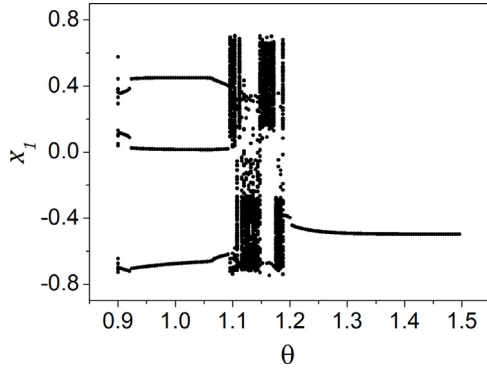
Fig. 5. Bifurcation diagrams varying θ with $\omega = 0.5$, $\gamma = 0.02$ and $\zeta = 0.05$.

The strain of the two bars of length L with respect to a reference length L_0 is expressed by:

$$\epsilon = \frac{L}{L_0} - 1 = \frac{\cos(\varphi_0)}{\cos(\varphi)} - 1 \tag{16}$$

where φ_0 is a reference angle defined by the reference length L_0.

By using geometric and constitutive equations, Eqs. (13) and (16), on the equation of motion, Eq. (15), and assuming a harmonic external forcing $F = \Gamma \sin(\Omega t + \beta)$, where Γ is its amplitude, Ω its radial velocity and β is an initial phase, the equation of motion can be expressed in non-dimensional form as:

$$
\begin{aligned}
u'' = {} & \gamma \sin(\omega t^* + \beta) - \zeta u' + u\{-\left[\theta - 1 - 3\alpha_2 + 5\alpha_3\right] \\
& + \left[\theta - 1 - \alpha_2 + \alpha_3\right]\left[x_1^2 + s^2\right]^{-\frac{1}{2}} - \left[3\alpha_2 - 10\alpha_3\right]\left[x_1^2 + s^2\right]^{\frac{1}{2}} \\
& + \left[\alpha_2 - 10\alpha_3\right]\left[x_1^2 + s^2\right] + 5\alpha_3\left[x_1^2 + s^2\right]^{\frac{3}{2}} - \alpha_3\left[x_1^2 + s^2\right]^2\}
\end{aligned} \tag{17}
$$

where $\gamma = \frac{\Gamma}{L_0 \Omega_0^2}$ is a non-dimensional amplitude, ζ is an non-dimensional viscous dissipation, $\omega = \frac{\Omega}{\Omega_0}$ is an non-dimensional angular velocity,

$u = \frac{U}{L_0}$, $t^* = t\Omega_0$, $\Omega_0 = \frac{2Aa_1 T_M}{mL_0}$, $s = \frac{S}{L_0}$, $\alpha_2 = \frac{a_2}{a_1 T_M}$, $\alpha_3 = \frac{a_3}{a_1 T_M}$, $\theta = \frac{T}{T_M}$ and $(\ )' = \frac{d}{dt^*}$.

It is worthful to mention that this SMA two-bar truss was previously investigated by Savi et al. [9] and Savi and Nogueira [10]. The first reference considers the polynomial model while the second one considers a more realistic constitutive model, employing internal variables, that properly describes the hysteretic behaviour. Both descriptions present the same qualitative truss behaviour. This means that the polynomial model together with a linear viscous dissipation is representative of the dynamical aspects of the SMA structural system.

4. Thermal actuation

The control of the SMA two-bar truss is carried out considering a controller based on the extended time-delayed feedback control method (ETDF) [17]. Velocity u' is assumed to be the observable variable, $y = u'$ as well as the only accessible state to apply the control. Under this assumption, the control signal $\boldsymbol{g} \in \mathbb{R}^N$, related to Eq. (2), becomes:

$$\boldsymbol{g} = \boldsymbol{K}\left[[1 - R]\sum_{j=1}^{\infty} R^{j-1}u'\left(t^* - j\tau\right) - u'\left(t^*\right)\right] \tag{18}$$

where $\boldsymbol{K} = [0 \ K]^T$ and $\boldsymbol{g} = [0 \ g]^T$.

It is important to distinguish the actuation force provided by the SMA elements, F_{act}, and the control signal g calculated by the ETDF method. Ideally, it is desirable that $F_{act} = g, \forall t^*$, however, this is not always true due to actuation constraints. By assuming a reference temperature, θ_{ref}, and that actuation is provided only by temperature changes on the SMA elements, Eq. (17) can be rewritten using state variables, $[x_1 x_2] = [u \ u']$, as follows:

$$
\begin{aligned}
x_1' = {} & x_2 \\
x_2' = {} & \gamma \sin(\omega t^* + \beta) - \zeta x_2 + x_1 \{ -\left[\theta_{ref} - 1 - 3\alpha_2 + 5\alpha_3\right] \\
& + \left[\theta_{ref} - 1 - \alpha_2 + \alpha_3\right]\left[x_1^2 + s^2\right]^{-\frac{1}{2}} - \left[3\alpha_2 - 10\alpha_3\right]\left[x_1^2 + s^2\right]^{\frac{1}{2}} \\
& + \left[\alpha_2 - 10\alpha_3\right]\left[x_1^2 + s^2\right] + 5\alpha_3\left[x_1^2 + s^2\right]^{\frac{3}{2}} - \alpha_3\left[x_1^2 + s^2\right]^2 \} + F_{act}
\end{aligned} \tag{19}
$$
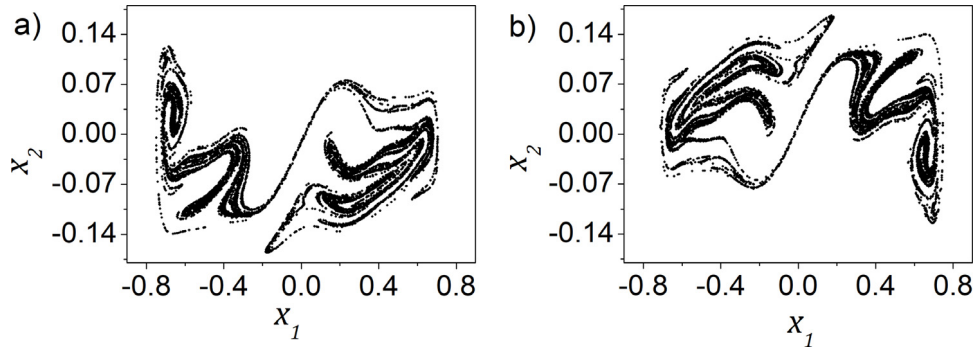
Fig. 6. Chaotic attractor for $\omega = 0.5$, $\theta = 1.1$, $\gamma = 0.02$ and $\zeta = 0.05$. (a) Poincaré section for zero valued motor phase. (b) Poincaré section with a phase shift of π.
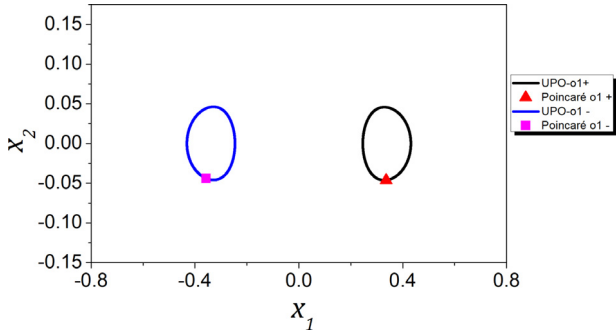
Fig. 7. Unstable periodic orbits of period-1 identified. Note that for each UPO there is a mirrored counterpart.
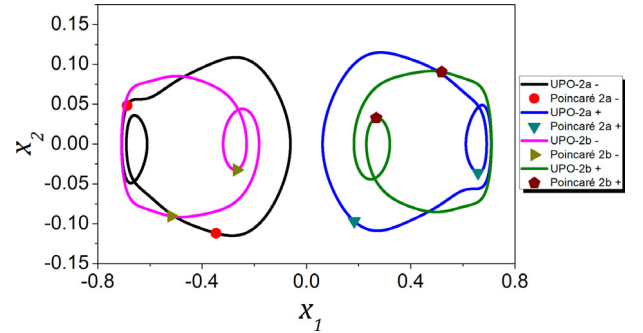
Fig. 8. Unstable periodic orbits of period-2 identified. Note that for each UPO there is a mirrored counterpart.

where,

$$F_{act} = x_1 \left[\left[\theta - \theta_{ref} \right] \left[\left[x_1^2 + s^2 \right]^{-\frac{1}{2}} - 1 \right] \right] \quad (20)$$

Note that there are three conditions where Eq. (20) vanishes regardless the temperature θ: $x_1 = \sqrt{1 - s^2}$, $x_1 = -\sqrt{1 - s^2}$, $x_1 = 0$. This can be understood as a geometric constraint of the controller, being associated with positions where the SMA bars have no strain and do not have any reaction force (the two first cases), or with the horizontal configuration of the truss where the SMA elements cannot apply any force on the vertical direction (last case).

Two controllers are now defined by considering thermal constraints. The ideal controller has the temperature θ as its accessible parameter and can provide any control force needed by the control strategy. On the other hand, the constrained controller changes the temperature of the SMA elements with an accessible electric current via Joule effect, being constrained by the energy equation. Therefore, the constrained controller is limited by heat transfer issues and cannot provide the calculated control signal estimated by the ETDF method while the ideal one uses exactly the estimated control signal.

Temperature variation that defines constrained controller actuation is provided by the Joule effect and therefore, current I is the accessible parameter. Hence, energy equation governs temperature variations and constraints actuation. Energy dissipation is provided only by convection phenomenon which governs cooling processes. It is assumed that the SMA elements have a constant resistance regardless the phase transformations and strains. Based on that, the energy equation is written as follows,

$$\dot{T} = \frac{h}{C_p} \left[T_E - T \right] + \frac{R}{C_p} I^2 \quad (21)$$

where C_p is the thermal capacity of the SMA, T_E is the ambient temperature R is the SMA resistance and h is the convection coefficient already accounting for the truss surface area.
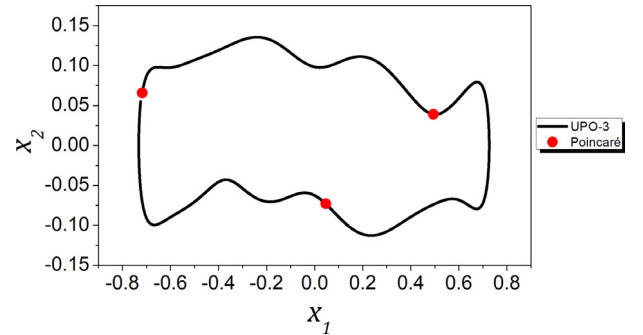
Fig. 9. Unstable periodic orbits of period-3 identified.
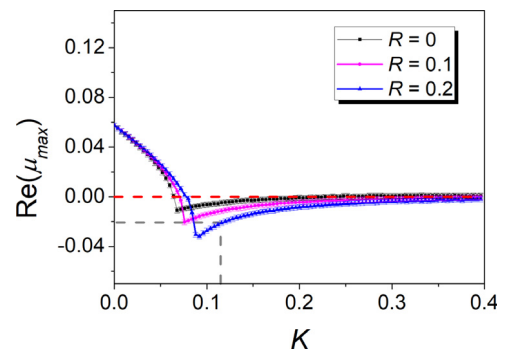
Fig. 10. Analysis of period-2 UPO Floquet exponents for different values of controller parameters K and R. The accuracy of Floquet exponent real values are of ± 0.002. The $\mathrm{Re}(\mu_{max})$ line is presented in dashed red, and the K value chosen for the control on dashed grey line. (For interpretation of the references to colour in this figure legend, the reader is referred to the web version of this article.)
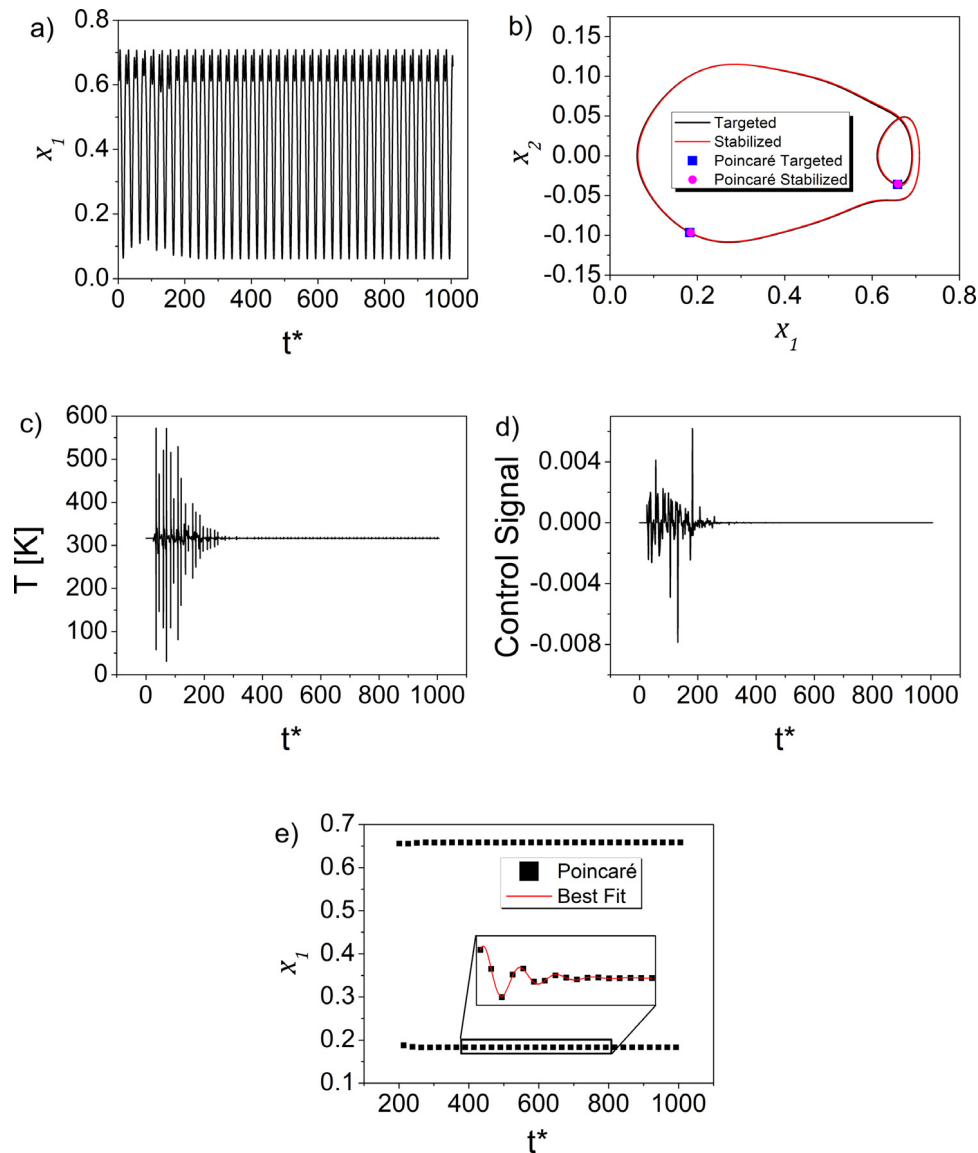
Fig. 11. Control of the positive UPO 2a for the ideal controller. (a) Position versus time. (b) Stabilised and targeted orbits. (c) Temperature versus time. (d) Control Signal versus time. (e) Poincaré section of position versus time.

The non-dimensional form of the energy equation is written as follows:

$$\theta' = h^* \left[\theta_E - \theta\right] + R_r I_r^2 \tag{22}$$

where $h^* = \frac{h}{C_p \Omega_0}$ is non-dimensional convective coefficient, $R_r = \frac{R I_0^2}{\Omega_0 C_p T_M}$ is a non-dimensional resistance of the bars, $\theta_E = \frac{T_E}{T_M}$ is the non-dimensional ambient temperature, I_0 is a reference current and $I_r = \frac{I}{I_0}$ the non-dimensional current.

Energy equation limits the accessible temperatures and the actuation force. The first part of the equation governs the cooling process as h^* defines how fast it can happen and cannot be accessed by the controller. The second part of the equation, on the other hand, controls heating and can be accessible by the current I_r that is limited to a maximum value. Hence, the constrained controller applies heating to the SMA elements, restricted by the current maximum value, but cooling process is governed just by convection.

The difference between ideal and constrained controllers can be established by an error defined by the difference between the actuation force of the constrained controller, F_{act}, and the calculated control

signal, g, divided by the maximum control signal required:

$$e = \frac{F_{act} - g}{\max(g)} \tag{23}$$

Note that ideal control signal, g, is obtained from Floquet exponent by considering Eq. (2), where no thermal constraint is considered.

Both controllers deal with the geometric restrictions using the same strategy: if $\min\left(x_1 - \left\{\sqrt{1-s^2}, -\sqrt{1-s^2}, 0\right\}\right)^2 < 10^{-3}$ the controller is turned off, and after x_1 leaves the vicinity of these values the controller is turned on again.

5. Uncontrolled dynamics

A brief investigation of the SMA two-bar truss uncontrolled dynamics is carried out in order to design the extended time-delayed feedback control. A more complete analysis of the system dynamics can be found in [9]. All simulations employ the fourth order Runge–Kutta method with time steps that ensure an relative error of the state space modulus smaller than 10^{-6}. All simulations assume the following parameters taken from the literature and based on typical experimental values [9]:
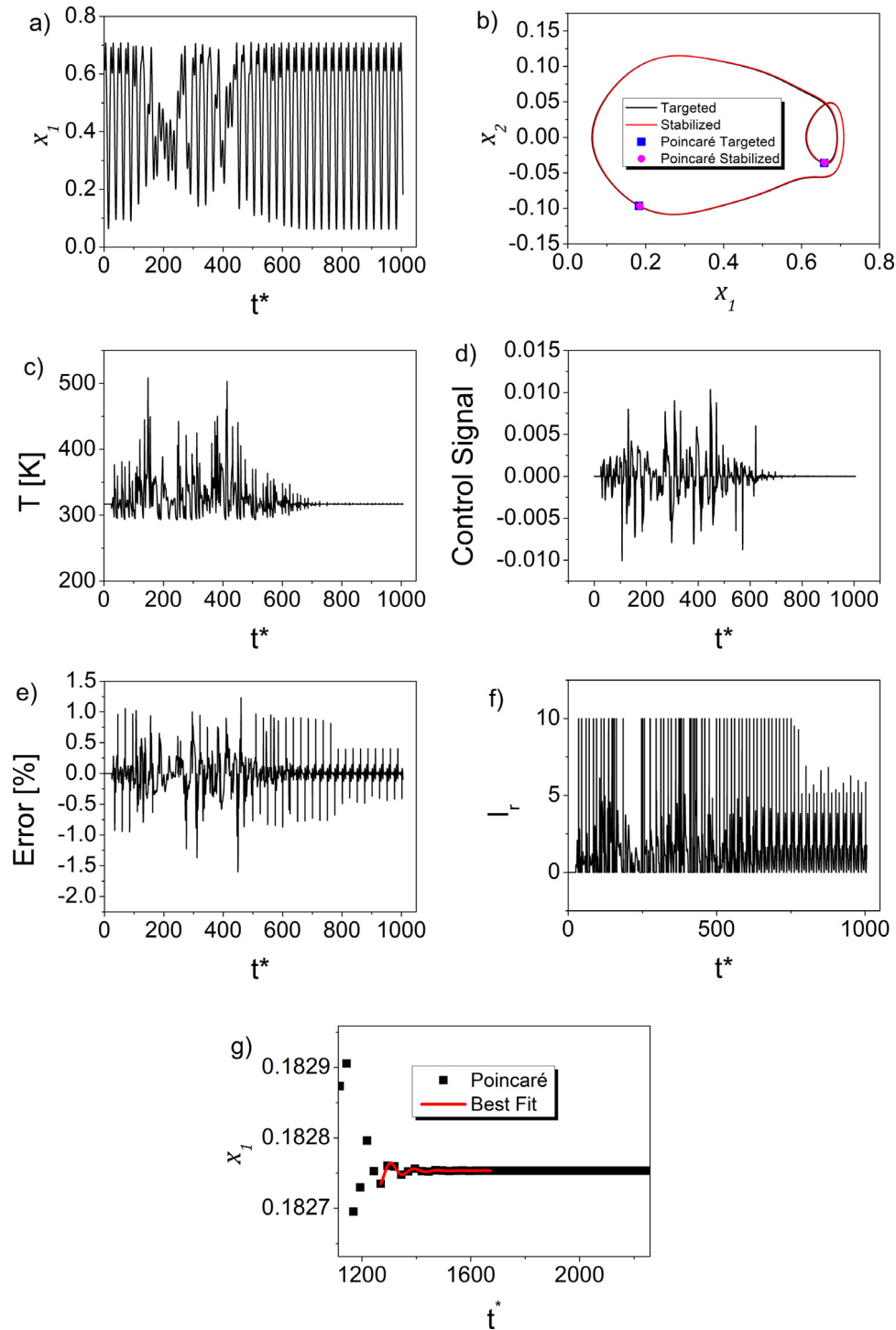
Fig. 12. Control of the positive UPO 2a for the constrained controller. (a) Position versus time. (b) Stabilised and targeted orbits. (c) Temperature versus time. (d) Control Signal versus time. (e) Control error versus time. (f) Current versus time. (g) Best fit of Poincaré section of position versus time.

$\alpha_2 = 1.24\ 10^2$, $\alpha_3 = 1.45\ 10^4$, $\theta_E = 1.017882$, $b = 0.866$, $R_r = 20$. All other parameters are defined for each simulation.

Initially, equilibrium point structure is analysed considering its temperature dependent behaviour. Fig. 3 presents equilibrium point locus as a function of temperature. Stability is evaluated from eigenvalues of the linearised system around each equilibrium point. At low temperatures ($\theta < 1$), there are two stable equilibrium points related to both stable martensitic phases; as temperature increases, austenite becomes stable being related to a pitchfork bifurcation of an unstable equilibrium point. Further temperature increases enable only austenite

to become stable causing the merge and destruction of stable and unstable equilibrium points. Therefore, high temperature behaviour of the SMA two-bar truss is similar to the one of the elastic counterpart. For low ($\theta < 1$) and intermediate temperatures ($1 < \theta < 1.265$), SMA constitutive nonlinearities introduces new equilibrium points.

A global comprehension of system dynamics can be achieved by considering bifurcations diagrams varying temperature, θ, and forcing amplitude, γ, parameters. Due to symmetric characteristics with respect to change of coordinates $x_1 \rightarrow -x_1$, it is expected that every orbit that is
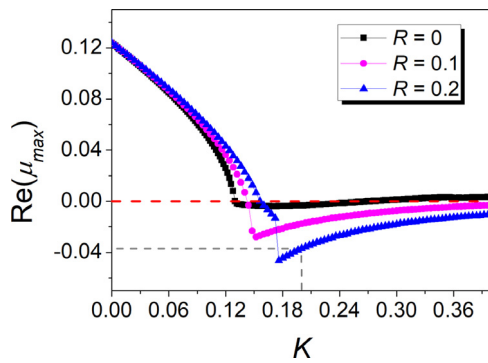
Fig. 13. Analysis of period-1 UPO Floquet exponents for different values of controller parameters K and R. The accuracy of Floquet exponents real values are of ± 0.002. The $\mathrm{Re}(\mu_{max})$ line is presented in dashed red, and the K value chosen for the control on dashed grey line. (For interpretation of the references to colour in this figure legend, the reader is referred to the web version of this article.)

Table 1
Floquet exponents of the identified UPOs. The negative counterparts have the same Floquet exponents due to the system symmetry.

UPO1+		UPO 2b+	
μ_1	μ_2	μ_1	μ_2
$0.124 + 0.25i$	$-0.174 + 0.25i$	$0.088 + 0.125i$	$-0.138 + 0.125i$
UPO 2a+		UPO 3	
μ_1	μ_2	μ_1	μ_2
$0.057 + 0.125i$	$-0.107 + 0.125i$	0.002	-0.04

asymmetric with respect to the coordinates transformation has a 180° rotated counterpart.

Fig. 4 shows different bifurcation diagrams varying the excitation amplitude γ. Three cases are presented: $\omega = 0.14$, $\theta = 1.3$ and $\zeta = 0.01$; $\omega = 0.1$, $\theta = 1.3$ and $\zeta = 0.01$; $\omega = 0.5$, $\theta = 1.1$ and $\zeta = 0.05$. Different initial conditions are considered and it should be pointed out that there are always at least two coexisting orbits, symmetrical with respect to $x_1 = 0$. Moreover, two kinds of chaotic regions are identified: the first type occurs for low values of γ, where the orbit is confined to positive or negative values of x_1; the second type is a region for greater values of γ that includes positive and negative values of x_1. Periodic regions can be identified between the chaotic ones.

The temperature variation is considered in Fig. 5. For temperatures below $T_M (\theta < 1)$ the system presents a period-3 response. Afterwards, chaotic response starts around $\theta = 1.1$, and finally, a period-1 response is identified for values greater than $\theta = 1.2$. The bifurcation diagram shows how temperature changes on SMA elements can alter the system response in different ways, indicating the adaptive SMA behaviour and its ability to induce periodic or chaotic behaviours.

Chaotic response is now of concern considering $\theta = 1.1$, $\omega = 0.5$, $\zeta = 0.05$ and $\gamma = 0.02$. The estimation of Lyapunov exponents assures the chaotic characteristic of system response. By employing the algorithm due to Wolf et al. [37], the following values are obtained: $\lambda_1 = 0.1172\,\mathrm{bit/s}$ and $\lambda_2 = -0.1854\,\mathrm{bit/s}$. Poincaré section of this behaviour is presented in Fig. 6, showing fractal structure in two different positions.

The analysis of the unstable periodic orbits (UPOs) embedded in chaotic attractor can be performed considering the recurrent points method [38]. The analysis is carried out considering a Poincaré section with 20,600 points, discarding the first 600 points. This method looks for periodic orbits scanning the time series, establishing a comparison with respect to tolerance parameters for the search: $r_1 = 0.04$ and $r_2 = 0.08$. Results of UPO identification are presented in the next three pictures. Fig. 7 shows two period-1 UPOs, which are small amplitudes symmetric orbits. Fig. 8 shows two pairs of period-2 UPOs. Fig. 9 shows a period-3 UPO that is around all the equilibrium points.

Floquet exponents of each one of the identified UPO are now calculated using the direct method [28], and results are presented in Table 1. Note that symmetric orbits have the same exponents and, therefore, only one is presented. It is also noticeable that each orbit has a positive and a negative exponent indicating the stable and unstable directions of the UPO.

6. Stabilisation of unstable periodic orbits

The chaos control method is now employed to stabilise UPOs that belong to the chaotic attractor. Initially, the control objective is to

stabilise the period-2a UPO previously discussed. The control parameters K and R are adjusted to be in the region that minimises the UPO Floquet exponents, calculated by the optimisation method. The reference temperature is set to be $\theta_{ref} = 1.1$. Fig. 10 considers the real part of the maximum real value of the Floquet exponent, $\mathrm{Re}\left(\mu_{max}\right)$, as a function of the parameter K considering the ideal controller and different values of R. Three values of K are important to be highlighted since it define the stability of the UPO: K_1 that is the lowest value of K where $\mathrm{Re}\left(\mu_{max}\right) < 0$; K_2 is the highest value of K where $\mathrm{Re}\left(\mu_{max}\right) < 0$; and K_{opt} where $\mathrm{Re}\left(\mu_{max}\right)$ is the minimum value. The values K_1 and K_2 can be observed by this method by evaluating when the curve intercepts zero (red dashed line), and K_{opt} is identified at the minimum of the curve. It is important to emphasise that the periodic orbit is stable on the region where $K_1 < K < K_2$.

Although Floquet exponents are estimated considering the ideal controller, these values are employed for both controllers. Control parameters are chosen, prior to the control application, in such a way to be near the minimum point of $\mathrm{Re}(\mu_{max})$: $K = 0.115$ and $R = 0.2$. The infinite sum of Eq. (18) is considered to converge on the first 10 terms (fast converging series assumption). The first delayed term of the system is simulated for 2 periods without control actuation and afterwards, the control is turned on. As time progresses, other terms are added with the nth delayed term been incorporated to the sum of Eq. (18) after n-periods are simulated.

Fig. 11 shows results for the period-2a UPO control considering the ideal controller while Fig. 12 shows results of the same UPO considering constrained controller with $h^* = 0.7$. Results show that both controllers achieve UPO stabilisation. Note that although no thermal constraint is considered in Floquet exponent calculation, used to define the values of K and R, constrained controller is able to stabilise the UPO. The ideal controller stabilises the targeted UPO faster and with a smaller control signal than the constrained one. The control signal almost vanishes on both controllers after stabilisation and the temperature on the ideal controller stabilises around the reference temperature while the constrained controller has some small fluctuations around the reference temperature. These variations may be due to the actuation limitations on the constrained controller evidenced by the actuation error that does not vanish completely after stabilisation. Finally, the constrained actuation suffers temperature changes of 200 K that are more feasible than the ideal controller variations ranging from 30 K to almost 600 K. Figs. 11e and 12g presents the Poincaré section for the state variable x_1 showing an exponential decay envelope on its details. In order to confirm the Floquet exponents calculated previously by the optimisation method, a sine function with an exponential decay is fitted on the Poincaré section time series. By following the time series method, the maximum real value of Floquet exponent is obtained for the ideal controller $\mathrm{Re}\left(\mu_{max}\right) = -0.018 \pm 0.001$, and for the constrained controller $\mathrm{Re}\left(\mu_{max}\right) = -0.015 \pm 0.001$. As expected, the predicted $\mathrm{Re}\left(\mu_{max}\right)$ agrees with exponent obtained of Fig. 10 within the fitting precision for the ideal controller, while the constrained controller has an increase of $\mathrm{Re}\left(\mu_{max}\right)$ indicating the influence of actuation constraints.

A period-1 UPO is now investigated. Initially, consider the evaluation of control parameters presented from the Floquet exponents analysis for different values of K and R for ideal controller, presented in Fig. 13.
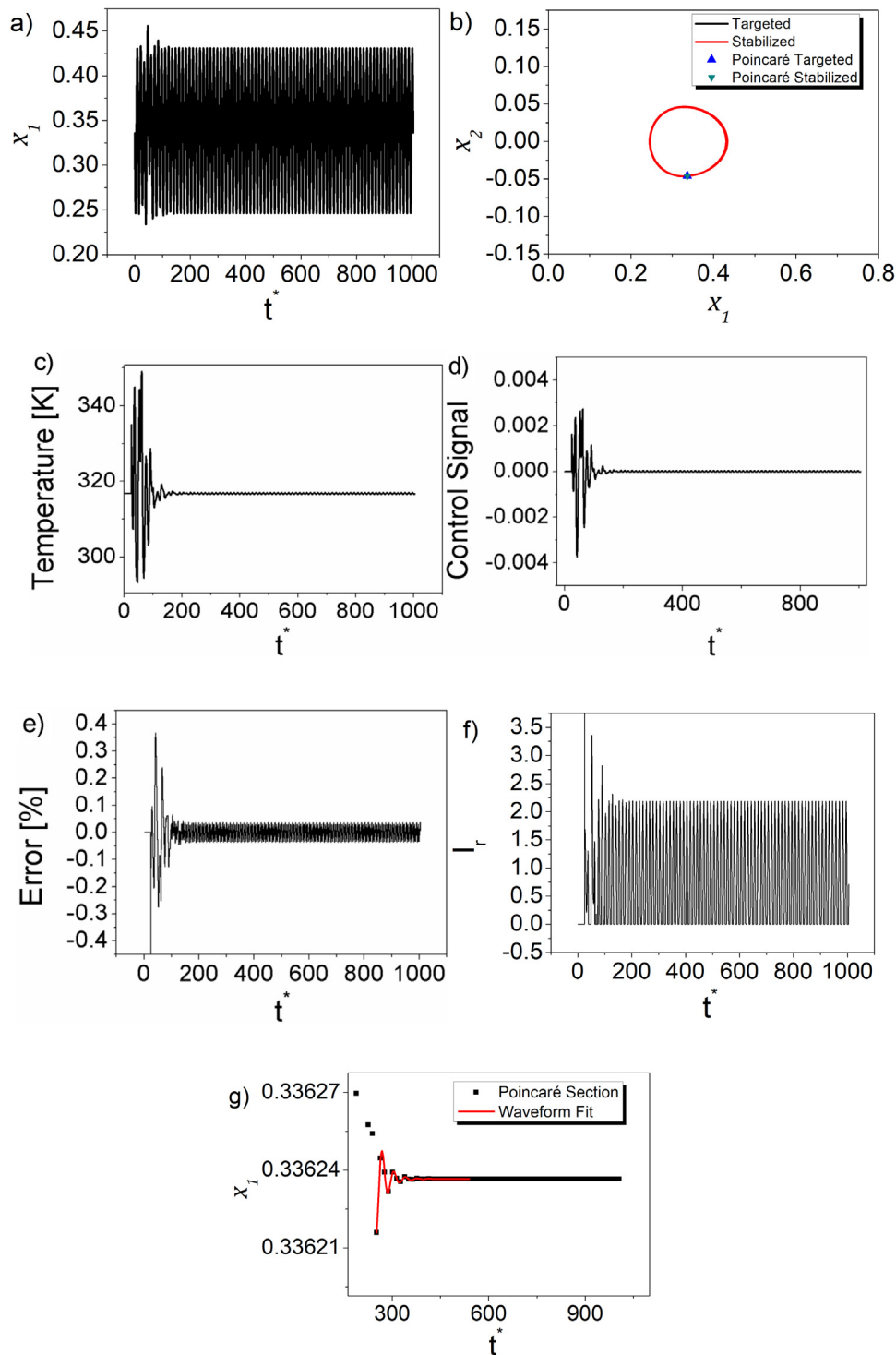
Fig. 14. Control of the positive period-1 UPO for the constrained controller. (a) Position versus time. (b) Stabilised and targeted orbits. (c) Temperature versus time. (d) Control Signal versus time. (e) Control error versus time. (f) Current versus time. (g) Best fit of Poincaré section of position versus time.

Control parameters are chosen in such a way to be near the minimum point of $\mathrm{Re}(\mu_{max})$: $K = 0.2$ and $R = 0.2$. This result is employed to the constrained controller in order to stabilise the UPO.

Fig. 14 presents results for the constrained controller assuming $h^* = 0.7$. Results show the stabilisation of the period-1 UPO with maximum temperature variations of 60 K and electric currents up to 3.5. The error obtained stays less than 0.4% excluding the initial control signal that may indicate that the constraints have small influence on this stabilisation. This is verified on Fig. 14g where the Floquet exponent obtained by the

fitting of a damped sine wave is equal to $\mathrm{Re}\left(\mu_{max}\right)$ previously calculated for the ideal controller resulting in $\mathrm{Re}\left(\mu_{max}\right) = 0.036 \pm 0.002$.

The influence of the convection parameter h^* is now in focus to evaluate the details about heat transfer constraints on the controller. Initially, the influence of h^* on the stability of the controlled period-2 UPO is investigated considering $\gamma = 0.02$ and $\omega = 0.5$ with control parameters $R = 0.2$ and $K = 0.115$. A bifurcation diagram is built starting at $h^* = 0.7$, case treated on Fig. 12, and then slowly decreasing h^* to zero (Fig. 15). This procedure sets the best scenario for the
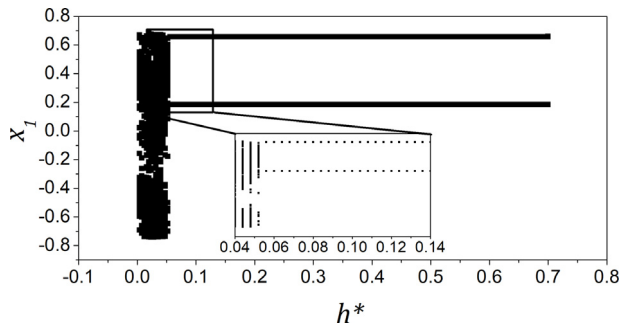
Fig. 15. Bifurcation diagram for the control of the period-2 UPO with varying h^*.
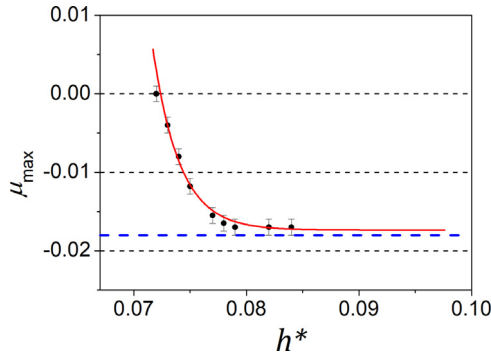
Fig. 16. Period-2 UPO maximum Floquet exponent real value for various values of h^*. In red is the best exponential fit of the data. The blue dashed line is the Floquet exponent value for the ideal controller.
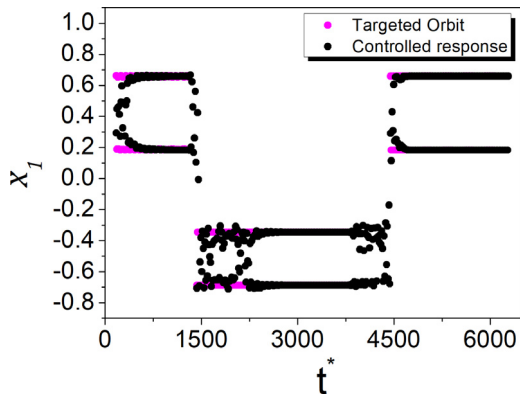
Fig. 17. Adaptive control of the SMA two-bar truss. In the transition periods were there is no displayed targeted orbit the control is turned off.
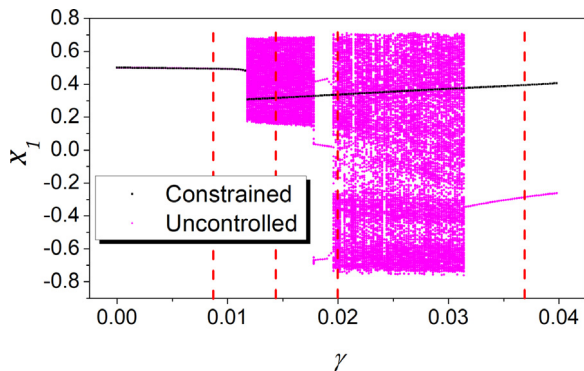
Fig. 18. Bifurcation diagram of uncontrolled system (magenta) and controlled system (black). The red lines indicate the values where the orbits of Fig. 18 are obtained. (For interpretation of the references to colour in this figure legend, the reader is referred to the web version of this article.)

controller as the UPO is already stabilised when the system slowly changes the parameter. Results show that the controller can stabilise the system until $h^* = 0.056 \pm 0.008$ (in detail of Fig. 15), when there is an abrupt change from the period-2 UPO to a chaotic behaviour.

A second analysis is carried out evaluating the exponential fit of the Floquet exponents versus h^* extracted by the time series method. Fig. 16 shows the best curve indicating that the orbit becomes unstable (Floquet exponents become positive) with values of h^* below 0.072 ± 0.001, which has just a small discrepancy with the previous analysis. This discrepancy is explained by the fact that the bifurcation diagram is performed exactly on the orbit within the simulation precision while the analysis of the Floquet exponents requires some displacement of the orbit slightly changing the initial conditions. Fig. 16 also shows that as h^* increases, the constrained controller tends to have the same μ_{max} as the ideal controller (blue dashed line). This result agrees with the same analysis made previously on the literature [23].

Note that stabilised UPOs in this work are chosen to show effectiveness of control method in avoiding chaotic behaviour. The ability of stabilising different UPOs, and the presence of an infinite number of UPOs embedded in chaos, makes this kind of response a flexible behaviour in the presence of control. In the case of the analysed two-bar truss, chaos control can be used to avoid snap through behaviour or mitigate vibration amplitudes of the system by stabilising appropriate UPOs.

7. Exchangeable target control

Chaos control approach can be employed to confer flexibility to the system since it allows a target exchange with low power consumption. This can promote structure configuration exchange and the strategy is to use the ETDF method to control two different target orbits representing two different structure configurations. Constrained controller is employed on all simulations.

The idea of target exchanges is illustrated considering period-2a UPO discussed on Section 6, Figs. 10–12, and its reflected counterpart. The exchange is performed considering two different period-2 UPO: period-2a+ and period-2a−, respectively associated with positive and negative displacements. Initially, a period-2a+ UPO is targeted for the first 100 periods using the same parameters employed on Section 6 ($K = 0.115$ and $R = 0.2$). Afterwards, the control is turned off and the system is free to leave the period-2 response. When the system reaches negative displacements, the control is turned on again for the next 200 periods, with the same parameters, which means that it is now targeting the period-2a− UPO. After that, the control is turned off again and turned when positive displacements are reached, stabilising the system in the previous period-2a+ UPO.

Fig. 17 shows the Poincare map time history for this control strategy. Note the controller ability to stabilise each targeted UPO, allowing the structure to oscillate in different configurations. This strategy shows that the ETDF method can stabilise multiple target orbits with the same parameters and hence, can provide structure adaptability by turning the control on and off.

8. Bifurcation control

In general, qualitative dynamical changes on bi-stable structures are critical as they usually mean a structure configuration change and can produce higher dynamical loads. In other words, it is desirable to a smart structure to stay on a desired low amplitude periodic behaviour than other dynamical response regardless of the applied external excitation and only change its configuration when required. In this regard, a bifurcation control can be applied to these structures and the ETDF method is a candidate to perform this kind of control.

The constrained controller is now employed to deal with bifurcation control. Bifurcations diagrams are considered assuming a quasi-static variation of parameter γ, with $\theta = 1.1$ and $\zeta = 0.05$, and initial conditions
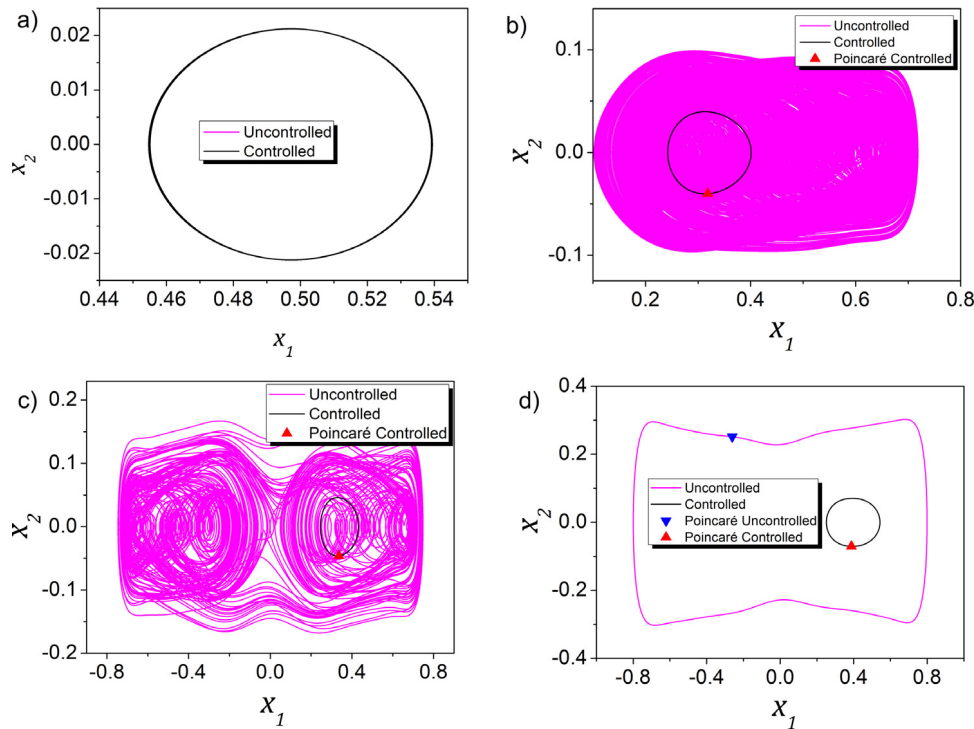
Fig. 19. State space of controlled and uncontrolled responses of Fig. 17. (a) $\gamma = 0.01$ (b) $\gamma = 0.015$ (c) $\gamma = 0.02$ (d) $\gamma = 0.035$.

$x_1(0) = 0.5$ and $x_2(0) = 0$. The parameter γ is initially zero and it is gradually increased as time evolves. The controller parameters are set to be $K = 0.2$ and $R = 0.2$ for the period-1 UPO. These values are designed for a standard value of $\gamma = 0.02$, being the same as previously mentioned for both UPOs.

Fig. 18 plots together bifurcation diagrams with and without control. The controlled diagram considers the stabilisation of the period-1 UPO. Fig. 19 presents different system responses for 4 values of γ, also highlighting the comparison between controlled and uncontrolled responses. Initially, the uncontrolled system has a period-1 response (Fig. 20a) for low values of γ. Above $\gamma = 0.0118$, the uncontrolled response presents a chaotic behaviour restricted to positive values of x_1 (Fig. 19b). After $\gamma = 0.018$, a periodic window appears between two chaotic regions and after $\gamma = 0.0196$ the chaotic attractor expands to negative values of the position x (Fig. 19c). Finally, at $\gamma = 0.0325$, the chaotic behaviour is replaced to a high amplitude period-1 orbit (Fig. 19d). On the other hand, the controlled system stays on the same periodic response as the uncontrolled system (Fig. 19a) until the uncontrolled system reaches the chaotic behaviour. At this transition, the controlled system stabilises on the targeted UPO and presents the same behaviour for the rest of the diagram (Fig. 19b,c,d).

âĂÍâĂÍ

Bifurcation control is also applied to the period-2a UPO. The controller parameters are set to be $K = 0.115$ and $R = 0.2$ as obtained in the preceding section. Fig. 20 overlaps results of the uncontrolled and controlled systems. The uncontrolled system has the same behaviour already described on the previous diagram. The controlled system stays in a periodic orbit (Fig. 21a) until a chaotic response is reached (Fig. 21b). In this region ($0.0116 \leq \gamma \leq 0.0186$), the uncontrolled system has an attractor slightly wider than the controlled one. Afterwards, close to the region where the control is designed, the period-2 UPO is stabilised on the controlled systems, which stays in this orbit for some values of γ (Fig. 21c). Increases in γ, make the controller lose the ability to stabilise the system, and a chaotic behaviour is reached, but still constrained to positive values of x_1. By increasing even more the value of γ makes the controlled system to present a high amplitude response ($\gamma \sim 0.023$). Further increases also make the controlled system pass
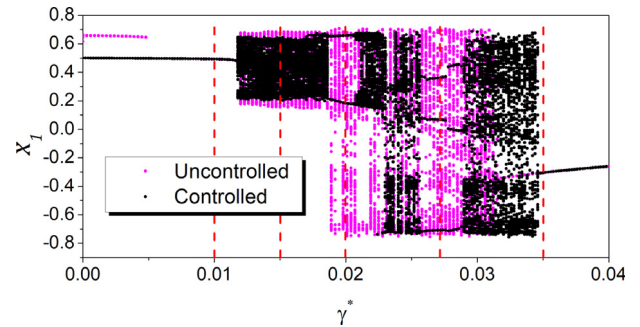
Fig. 20. Bifurcation diagram of uncontrolled system (magenta) and controlled system (black). The red lines indicate the values where the orbits of Fig. 21 are obtained. (For interpretation of the references to colour in this figure legend, the reader is referred to the web version of this article.)

through another periodic window (Fig. 21d) and finally with $\gamma \sim 0.035$ the chaotic behaviour stops (Fig. 21e). It should be pointed out that the chaotic behaviour of the uncontrolled system stops at $\gamma \sim 0.032$, before the controlled one. In order to verify if the controller is able to stabilise the UPO for previous values of $\gamma < 0.02$, a backward bifurcation is performed after the system is stabilised on the UPO, generating the best scenario to the controller. The verification showed no discrepancies between the two bifurcation diagrams.

The convection parameter h^* influence on system response is now of concern evaluating the width of the controlled periodic window around $\gamma = 0.02$ of Fig. 20. This width can be related to the ability of the controller to stabilise the system on different forcing conditions. Fig. 22 shows the widths of these windows for various values of h^*. As the parameter decreases its value, the window width also decreases but on a seemingly linear matter.

9. Conclusions

Chaos control of an SMA two-bar truss is performed using the extended time-delayed feedback approach. Floquet exponents are used
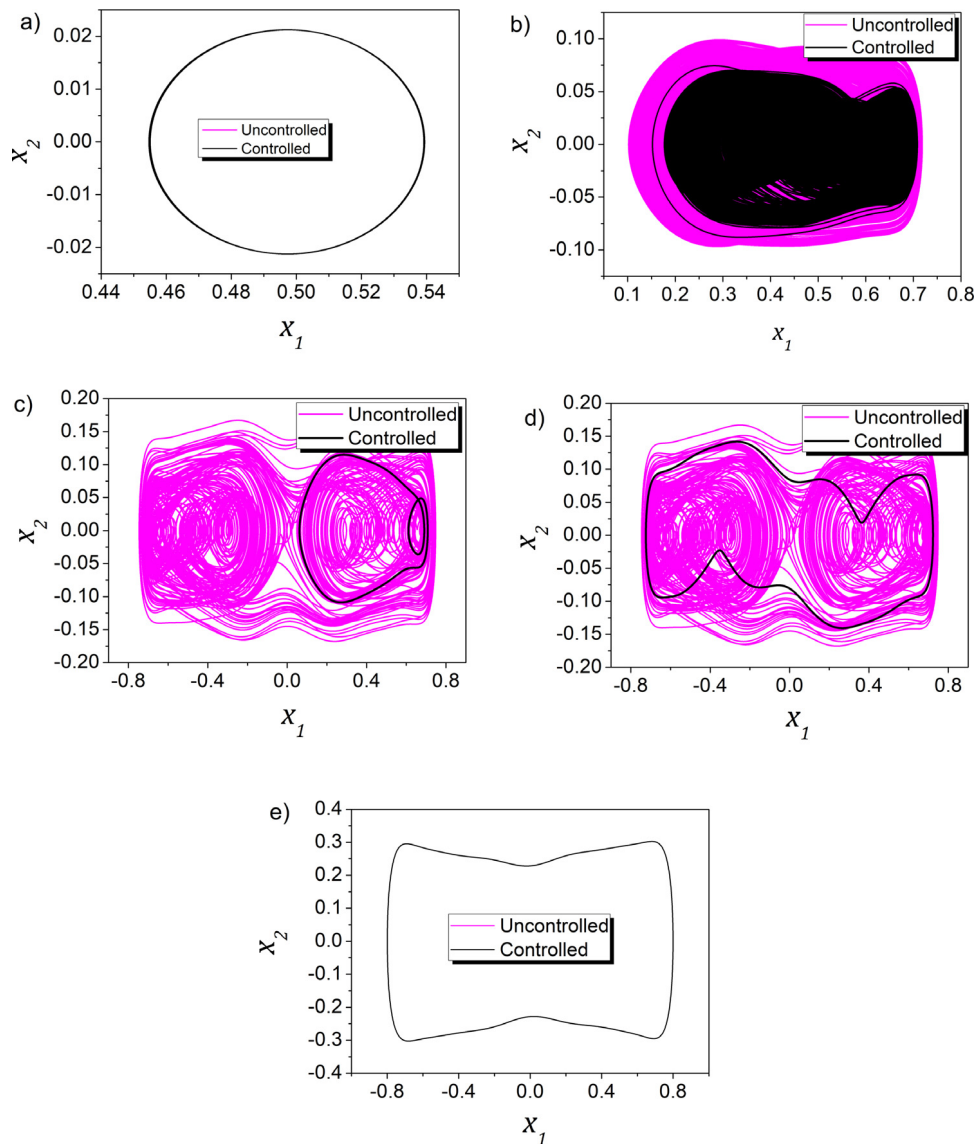
Fig. 21. State space of controlled and uncontrolled responses of Fig. 20. (a) $\gamma = 0.01$ (b) $\gamma = 0.015$ (c) $\gamma = 0.02$ (d) $\gamma = 0.0288$ (e) $\gamma = 0.04$.
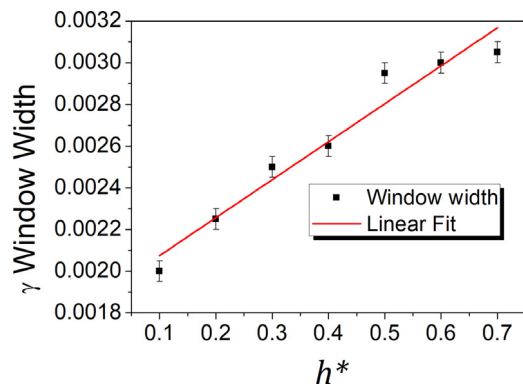
Fig. 22. Periodic window width for various values of h^*.

to set control parameters and to compare ideal and thermal constrained controllers. Results show that thermal actuation of SMA elements can be employed to either stabilise UPOs embedded in the chaotic attractor or to perform bifurcation control. Comparisons between ideal

and constrained controller show that thermal constraints are directly associated with the convection coefficient, and both controllers have the same behaviour for high values of this coefficient. This conclusion may be assured by observing the Floquet exponents that are similar for this condition. Target orbit exchange is exploited showing that this strategy can confer flexibility to the system response, promoting exchanges among different, desirable orbits. Another potential application of the chaos control strategy is the bifurcation control. This is performed with constrained controller showing that SMA elements can provide thermal actuation to prevent dynamical changes. Results show that the effective window of stabilisation on a bifurcation diagram depends linearly with thermal constraints. In summary, this article shows that SMA can be successfully employed for chaos control even when thermal constraints are considered. This approach has different possibilities to smart structures including stability and configuration changes.

Acknowledgments

References

[1] E. Sitnikova, E. Pavlovskaia, J. Ing, M. Wiercigroch, Suppressing nonlinear resonances in an impact oscillator using SMAs, Smart Mater. Struct. 21 (2012) 075028.

[2] K. Kuribayashi, K. Tsuchiya, Z. You, D. Tomus, M. Umemoto, T. Ito, M. Sasaki, Self-deployable origami stent grafts as a biomedical application of Ni-rich TiNi shape memory alloy foil, Mater. Sci. Eng. A 419 (2006) 131–137.

[3] M. Salerno, K. Zhang, A. Menciassi, J.S. Dai, A novel 4-DOF origami grasper with an SMA-actuation system for minimally invasive surgery, IEEE Trans. Robot. 32 (2016) 484–498.

[4] B. Kim, M.G. Lee, Y.P. Lee, Y. Kim, G. Lee, An earthworm-like micro robot using shape memory alloy actuator, Sensors Actuators A 125 (2006) 429–437.

[5] S.M. Dutta, F.H. Ghorbel, Differential hysteresis modeling of a shape memory alloy wire actuator, IEEE/ASME Trans. Mechatronics 10 (2005) 189–197.

[6] A. Nespoli, S. Besseghini, S. Pittaccio, E. Villa, S. Viscuso, The high potential of shape memory alloys in developing miniature mechanical devices: a review on shape memory alloy mini-actuators, Sensors Actuators A 158 (2010) 149–160.

[7] M.A. Savi, Nonlinear dynamics and chaos in shape memory alloy systems, Int. J. Non-Linear Mech. 70 (2015) 2–19.

[8] Z.P. Bazant, L. Cedolin, Stability of Structures, Oxford University Press, Oxford, 1991.

[9] M.A. Savi, P.M. Pacheco, A.M. Braga, Chaos in a shape memory two-bar truss, Int. J. Non-Linear Mech. 37 (2002) 1387–1395.

[10] M.A. Savi, J.B. Nogueira, Nonlinear dynamics and chaos in a pseudoelastic two-bar truss, Smart Mater. Struct. 19 (2010) 115022.

[11] A.S. de Paula, M.A. Savi, Comparative analysis of chaos control methods: A mechanical system case study, Int. J. Non-Linear Mech. 46 (2011) 1076–1089.

[12] A.L. Fradkov, R.J. Evans, Control of chaos: Methods and applications in engineering, Annu. Rev. Control 29 (2005) 33–56.

[13] A.S. De Paula, M.A. Savi, V. Vaziri, E. Pavlovskaia, M. Wiercigroch, Experimental bifurcation control of a parametric pendulum, J. Vib. Control 23 (2017) 2256–2268.

[14] A.S. de Paula, M.V.S. dos Santos, M.A. Savi, W.M. Bessa, Controlling a shape memory alloy two-bar truss using delayed feedback method, Int. J. Struct. Stab. Dyn. 14 (2014) 1440032.

[15] A.S. De Paula, M.A. Savi, M. Wiercigroch, E. Pavlovskaia, Bifurcation control of a parametric pendulum, Int. J. Bifurcation Chaos 22 (2012) 1250111.

[16] S. Boccaletti, C. Grebogi, Y.-C. Lai, H. Mancini, D. Maza, The control of chaos: theory and applications, Phys. Rep. 329 (2000) 103–197.

[17] J.E.S. Socolar, D.W. Sukow, D.J. Gauthier, Stabilizing unstable periodic orbits in fast dynamical systems, Phys. Rev. E 50 (1994) 3245–3248.

[18] J. Lehnert, P. Hövel, V. Flunkert, P.Y. Guzenko, A.L. Fradkov, E. Schöll, Adaptive tuning of feedback gain in time-delayed feedback control, Chaos 21 (2011) 043111.

[19] K. Pyragas, W. Just, Global properties in an experimental realization of time-delayed feedback control with an unstable control loop, Phys. Rev. Lett. 98 (2007) 2141–2144.

[20] V. Pyragas, K. Pyragas, Act-and-wait time-delayed feedback control of autonomous systems, Phys. Lett. A 382 (2018) 574–580.

[21] A.S. de Paula, M.A. Savi, Controlling chaos in a nonlinear pendulum using an extended time-delayed feedback control method, Chaos Solitons Fractals 42 (2009) 2981–2988.

[22] W.O.V. Barbosa, A.S. De Paula, M.A. Savi, D.J. Inman, Chaos control applied to piezoelectric vibration-based energy harvesting systems, The Euro. Phys. J. Special Topics 224 (2015) 2787–2801.

[23] D.D.A. Costa, M.A. Savi, Chaos control of an SMA–pendulum system using thermal actuation with extended time-delayed feedback approach, Nonlinear Dynam. 93 (2018) 571–583.

[24] W.M. Bessa, A.S. de Paula, M.A. Savi, Chaos control using an adaptive fuzzy sliding mode controller with application to a nonlinear pendulum, Chaos Solitons Fractals 42 (2009) 784–791.

[25] A.S. de Paula, M.A. Savi, Chaos control applied to mechanical systems, Chaotic Model. Simul. (CMSIM) 1 (2012) 17–24.

[26] D.J. Christini, J.J. Collins, P.S. Linsay, Experimental control of high-dimensional chaos: The driven double pendulum, Phys. Rev. E 54 (1996) 4824–4827.

[27] A. Kittel, J. Parisi, K. Pyragas, Delayed feedback control of chaos by self-adapted delay time, Phys. Lett. A 198 (1995) 433–436.

[28] K. Pyragas, Delayed feedback control of chaos, Phylos. Trans. Roy. Soc. 364 (2006) 2309–2334.

[29] K. Pyragas, A. Tamaševičius, Experimental control of chaos by delayed self-controlling feedback, Phys. Lett. A 180 (1993) 99–102.

[30] W. Just, T. Bernard, M. Ostheimer, E. Reibold, H. Benner, Mechanism of time-delayed feedback control, Phys. Rev. Lett. 78 (1997) 203–206.

[31] R. Storn, K. Price, Differential evolution–a simple and efficient heuristic for global optimization over continuous spaces, J. Glob. Optim. 11 (1997) 341–359.

[32] D.C. Lagoudas, Shape Memory Alloys, first ed., Springer US, Boston, MA, 2008.

[33] A. Paiva, M.A. Savi, An overview of constitutive models for shape memory alloys, Math. Probl. Eng. 2006 (2006) 56876.

[34] F. Falk, Model free energy, mechanics, and thermodynamics of shape memory alloys, Acta Metall. 28 (1980) 1773–1780.

[35] M.A. Savi, P.M.C.L. Pacheco, Chaos and hyperchaos in shape memory systems, Int. J. Bifurcation Chaos 12 (2002) 645–657.

[36] D. Bernardini, G. Rega, Evaluation of different SMA models performances in the nonlinear dynamics of pseudoelastic oscillators via a comprehensive modeling framework, Int. J. Mech. Sci. 130 (2017) 458–475.

[37] A. Wolf, J.B. Swift, H.L. Swinney, J.A. Vastano, Determining Lyapunov exponents from a time series, Physica D 16 (1985) 285–317.

[38] D. Auerbach, P. Cvitanović, J.-P. Eckmann, G. Gunaratne, I. Procaccia, Exploring chaotic motion through periodic orbits, Phys. Rev. Lett. 58 (1987) 2387–2389.